Statistical Reconstruction of 3D Paper Structure Using Simulated Annealing Algorithm Based on 2D Scanning Electron Microscopy Image

Jie Xu, Yin Liu, Jiaqin Li, Wenhao Shen, Jean-Pierre Corriou

Journal of Natural Fibers

ISSN: (Print) (Online) Journal homepage: https://www.tandfonline.com/loi/wjnf20

Statistical Reconstruction of 3D Paper Structure Using Simulated Annealing Algorithm Based on 2D Scanning Electron Microscopy Image

Jie Xu, Yin Liu, Jiaqin Li, Wenhao Shen & Jean-Pierre Corriou

To cite this article: Jie Xu, Yin Liu, Jiaqin Li, Wenhao Shen & Jean-Pierre Corriou (2022) Statistical Reconstruction of 3D Paper Structure Using Simulated Annealing Algorithm Based on 2D Scanning Electron Microscopy Image, Journal of Natural Fibers, 19:16, 13815-13830, DOI: 10.1080/15440478.2022.2107141

To link to this article: https://doi.org/10.1080/15440478.2022.2107141

JOURNAL OF NATURAL FIBERS
2022, VOL. 19, NO. 16, 13815–13830
https://doi.org/10.1080/15440478.2022.2107141

Taylor & Francis
Taylor & Francis Group

Statistical Reconstruction of 3D Paper Structure Using Simulated Annealing Algorithm Based on 2D Scanning Electron Microscopy Image

Jie Xu[a], Yin Liu[a], Jiaqin Li[a], Wenhao Shen[a], and Jean-Pierre Corriou[b]

[a]State Key Laboratory of Pulp and Paper Engineering, South China University of Technology, Guangzhou, P.R. China; [b]Laboratoire Réactions et Génie des Procédés, UMR 7274-CNRS, Lorraine University, ENSIC, Nancy Cedex, France

ABSTRACT

The microstructure of fibrous paper plays an important role in its property investigation. In this study, an approach is proposed to extrapolate a 2D image into a virtual 3D microstructure. Five types of handsheets made of different pulps were prepared. Then, a hybrid function of two-point correlation and lineal-path function (S_2&L_2) and co-occurrence correlation functions (*CCFs*) was used in the simulated annealing reconstruction method. Thus, microstructures of two-phase fiber-pore handsheets were reconstructed using 2D scanning electron microscopy images. Finally, penetration simulations and calculations of the absolute permeability of handsheets were conducted. The statistical values of two-point correlation function (S_2) and lineal-path function (L_2) extracted from the reconstructed images were used to characterize the reconstruction accuracy, and the comparisons of reconstruction accuracy and time were made. The study results showed that the 3D microstructures of fibrous handsheets could be reconstructed effectively by S_2&L_2 and *CCFs*, identifying with the targets. The accuracies were around 10^{-5}, and the reconstruction times by *CCFs* were shortened by 30–60% compared with S_2&L_2. Moreover, the visual permeability simulation results could reflect the structural difference of handsheets, according to the calculated absolute permeability. These findings provide a guidance for 3D reconstruction of natural fiber paper.

摘要

本研究提出了一种由纸张的2D扫描电子显微镜 (SEM) 图像重建其3D微结构的方法。制备了5种纤维的手抄纸, 分别采用两点相关和复合线性路径函数 (S_2&L_2) 以及共现相关函数(*CCFs*) 的模拟退火方法,基于SEM图像, 重构了纸张的3D微观结构, 并用图像的S_2和L_2函数来表征重建精度, 最后进行了纸张渗透性能的模拟。结果表明, S_2&L_2和*CCFs*可以有效重建纸张3D微观结构, 重建精度约为10^{-5}; *CCFs*的重建时间比S_2&L_2缩短30%-60%;渗透模拟结果与计算的绝对渗透率保持一致。

KEYWORDS

Microstructure; three-dimensional reconstruction; paper sheets; simulated annealing reconstruction; simulation; permeability

Introduction

The porous fiber material is a classical type of functional material with a network structure. As a porous biomaterial, paper has a complex 3D anisotropic structure composed of fibers and pores (Ghassemzadeh and Sahimi 2004a, 2004b; Ghassemzadeh et al. 2001), whose pore structure is irregular, largely affecting its physical, optical, and transport properties (Costa et al. 2021; Du et al. 2021; Milanovic et al. 2020). Recently, owing to its renewability and recyclability, as a substitute to plastic products, paper has been continuously developed as functional materials, such as the materials

CONTACT Wenhao Shen ppwhshen@scut.edu.cn State Key Laboratory of Pulp and Paper Engineering, South China University of Technology, Guangzhou 510640, P.R. China

Supplemental data for this article can be accessed online at https://doi.org/10.1080/15440478.2022.2107141

for separation, filtration, and electrochemistry in petrochemical, medicine, and environmental protection areas (Schiller and Wang 2018; Wang and Gao 2021; Zhou et al. 2019), whose performance are greatly affected by their inherent pore network structures. Therefore, the determination of the fibrous microstructure of a paper sheet is critical for its physical and chemical properties.

Property studies based on the structure of the paper sheet are mainly conducted at macroscopic scale (Moura, Ferreira, and Figueiredo 2005), using the traditional experimental detection and theoretical analysis methods, which cannot quantify and visualize the relationship between the microstructure and property of paper sheet. With the development of computer simulation, the studies on the internal fiber-pore structure, fluid permeability (Taghiyari et al. 2019) and stress-strain (Lin, Bai, and Xu 2021) of paper sheet have been put forward.

For microstructure characterization, 2D imaging techniques involve scanning electron microscopy (SEM) and transmission electron microscopy (TEM), and 3D imaging techniques include focused-ion-beam scanning electron microscope (FIB-SEM) and X-ray computed tomography (CT). The comparisons of these techniques are summarized in S1 of Supplementary Information (SI). Alternatively, with the technical progresses of computer and scanning imaging, some novel reconstruction algorithms have emerged to generate 3D models (Sahimi and Tahmasebi 2021), for instance, to reproduce the pore structures of sandstone or solid oxide fuel cell electrodes (Gao et al. 2015; Zhang et al. 2019), by using experimental 2D high-resolution micrographs at low costs and flexible ways.

The 3D reconstruction can be realized by computer simulation with mathematical correlation functions to describe the statistical and topological properties of pore structure (pore space distribution, pore size) for porous materials. These statistical methods mainly include simulated annealing reconstruction (SAR) (Jiao, Stillinger, and Torquato 2009; Yeong and Torquato 1998a, 1998b; Zachary and Torquato 2011), Gaussian random fields reconstruction (Mukherjee and Wang 2006), and multiple-point statistics reconstruction (MPS) (Strebelle 2002; Tahmasebi and Sahimi 2012, 2013, 2016a, 2016b). The poor connectivity of the Gaussian random fields reconstruction limits its application. MPS mainly focuses on characterizing the correlation between multiple points, it has the unique advantages in dealing with long-distance connecting channels and characterizing some complex pore space shapes. However, there are high requirements for the initial 2D training images, and the continuity of the generative model needs to be improved.

In these 3D statistical reconstruction methods, SAR method is particularly attractive with regard to its ability to introduce various correlation functions to reconstruct the micropore structures for any type of porous material by minimizing the difference between target and reconstructed microstructures (Zhou and Xiao 2018). Moreover, in the SAR method, a number of *N*-point correlation functions have been developed to extract enough information from images, including two-point correlation function (Corson 1974), lineal-path function (Lu and Torquato 1992), and two-point cluster function (Jiao and Chawla 2014; Torquato, Beasley, and Chiew 1988). However, for the microstructure images in the cases of anisotropic, multiphase or large-format, the high calculation cost of SAR with *N*-point correlation functions is inevitable. To overcome the drawbacks of *N*-point correlation functions, developed from the gray-level co-occurrence matrix (GLCM) (Haralick, Shanmugam, and Dinstein 1973) in the texture analysis method, co-occurrence correlation functions (*CCFs*) (Feng et al. 2018) have been applied to microstructure reconstruction, which can effectively extract the structure characteristics of porous material (Kim et al. 2021).

All the aforementioned statistical reconstructions of 3D microstructure including SAR method are based on image information. Since the fiber porous material can be essentially regarded as a two-phase material, meaning that their binary images can be obtained in terms of images, it is theoretically possible to extend these reconstruction methods to various porous materials including paper sheet with different properties. Considering the similarity and difference of the microstructures between paper and other porous materials, in the study, the SAR method is applied as an initial attempt to reconstruct the 3D microstructure of fibrous paper, expecting to develop the 3D microstructure of paper sheet by the low-cost 2D image.

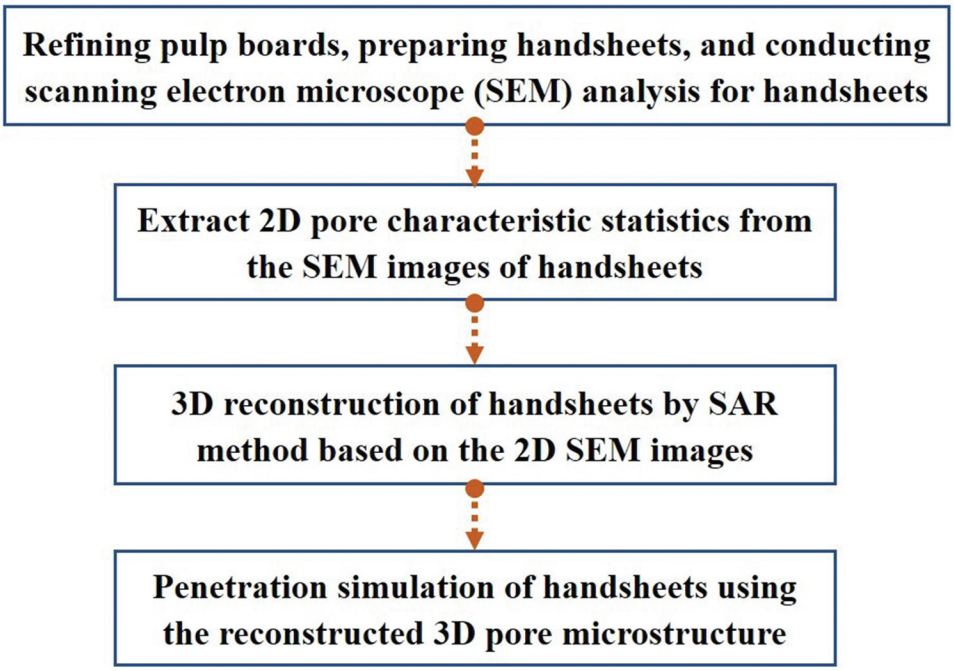

Figure 1. Roadmap of microstructure reconstruction for paper sheet.

Aiming to reconstruct the 3D microstructure of fiber-pore two-phase for paper sheet, the present study utilized a hybrid function of two-point correlation function and lineal-path function (S_2&L_2), and the *CCFs* function as the objective functions in SAR method, respectively. As shown in Figure 1, the study roadmap is explained as follows. Five different types of handsheets made of eucalyptus, masson pine, bamboo, bagasse, and cotton pulps were first prepared, and their 2D images were obtained by SEM analysis. Subsequently, using the 2D SEM images as inputs, the corresponding 2D and 3D porous models for different handsheets were constructed using the correlation functions of S_2&L_2 and *CCFs*, respectively. Their comparisons of reconstruction time and precision were also demonstrated conclusively. Eventually, based on the reconstructed 3D structures, the penetration processes of water in the porous structure of handsheets were simulated, and the absolute permeability of different fiber papers were calculated and compared. In the study, the applicability and validity with SAR method to reconstruct the pore structure of paper were revealed by the simulation results, providing the reliable simulation data for the development of functional paper as porous structural materials.

Experiment

To perform the 3D reconstruction of fiber paper with different raw materials, paper sheets with different pulp boards were made by a manual paper machine (TAPPI *T*-205), and then the 2D images of the paper sheets were obtained by SEM as the target image for reconstruction. Finally, the air permeability of the paper sheet was measured.

The experimental details are provided in S2 of SI, and all the reconstructions and simulations in the study were performed using a computer with Intel CPU i5–9300 H (2.40 GHz).

Methodology

Simulated annealing reconstruction for paper sheet

In the study, the basic method of SAR was first applied as the theoretical basis of the reconstruction of handsheet microstructure, then three correlation functions including two-point correlation function (S_2), lineal-path function (L_2) and co-occurrence correlation functions (*CCFs*) were employed individually to characterize the structural characteristics of handsheet.

"Image annealing" is the process of minimizing the statistical angle difference between the reconstructed image and the target image, namely, the process of reducing the system energy to a minimum. The flow chart of the simulated annealing reconstruction is illustrated in Figure 2, and the specific introductions of SAR and Figure 2 are put in S3 of SI.

The principles of the two-point correlation function $S_2^{(i)}(x_1, x_2)$ and the lineal-path function $L_2^{(i)}(x_1, x_2)$ are explained in S4 of SI (Fig. S2), and the principle of co-occurrence correlation functions (*CCFs*) to extract image morphological information is detailed in S5 of SI (Fig. S3).

Permeability simulation

Darcy's law based on experiments has been widely used in fluid research of porous media (Whitaker 1986), as illustrated in Eq. (S15). In Darcy's law, the absolute permeability k is defined as a measure of the ability of a porous material to transport a single-phase fluid. It is an inherent property of the material which is not influenced by external conditions. Moreover, in most applications of paper sheet, it mainly focuses on the transmission process of fluid in its thickness direction (Z-direction), such as filter materials (Pan et al. 2021), packaging barrier materials (Alexandersson and Ristinmaa 2021). In the present study, according to the actual situation, the boundary conditions of the simulation model for paper sheet are set as Figure 3, and the absolute permeability in the Z-direction (ZD) of the paper sheet was calculated with the numerical simulation based on computational fluid dynamics (CFD). The details of simulation are provided in S6 of SI.

Results and discussion

Two-dimensional reconstruction model of paper sheets

As shown in Figure 4, 2D structure images were obtained by SEM analysis. Then, the median filtering (Esakkirajan et al. 2011) and OTSU method (Poletti et al. 2012) were applied to denoise and binarize the images, respectively. Based on the binarized SEM images (Figure 5), using correlation functions S_2 &L_2 and *CCFs*, the two-dimensional reconstruction models were developed, respectively, and their reconstruction results were further compared.

2D reconstruction model with the correlation function S2&L2 and CCFs

Prior to the structure reconstruction with the correlation functions S_2&L_2 and *CCFs*, to balance the reconstruction accuracy and calculation speed, the suitable distances (r_d, r_l and r_{ccf}) of the two-point correlation function, lineal-path function and co-occurrence correlation functions were determined first. The details of distance determination are provided in S7.1 of SI (Figs. S4 and S5). In addition to the determination of distance, by a trial and error method, the other main simulated annealing parameters of S_2&L_2 and *CCFs* were also set as shown in Table 1.

Due to the space limitation, the example of the handsheet made of bagasse (Figure 5(d)) is considered, and its 2D reconstruction results with hybrid S_2&L_2 function and *CCFs* function are put in Figure 6 (the detailed process refers to S7.2 of SI).

It can be observed that the reconstruction results with hybrid S_2&L_2 function (Figure 6(b)) and *CCFs* function (Figure 6(c)) do not exactly represent the real microstructure (Figure 6(a)) from an intuitive point of view, which could not be quantitatively characterized in this visual way for judging

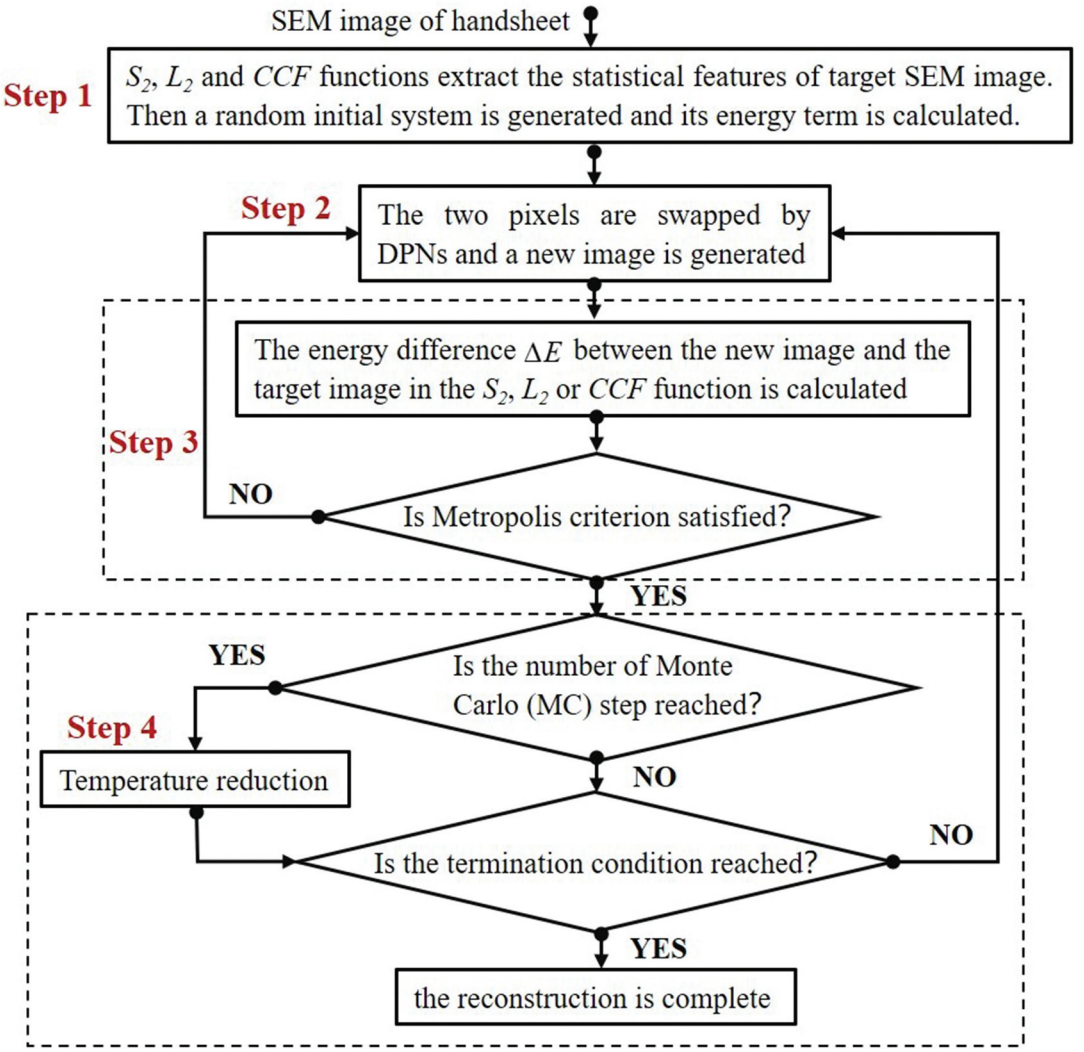

Figure 2. The flow chart of the simulated annealing reconstruction.

the accuracy of the S_2&L_2 method. In fact, it is universally acknowledged that S_2&L_2 is a reduced dimensional descriptor of microstructures (Zhang et al. 2019), and the similarity between the reconstructed and actual microstructures is often evaluated via some statistics of geometric properties, such as porosity, pore distribution, and connection (Wu and Jiang 2013).

Thus, in the present work, the statistical characteristics of pore structure (S_2 and L_2) in the images are used to quantitatively evaluate the difference between the target microstructure and the reconstructed results. Using Figs. 6(a–c) as the individual inputs, the statistical geometric properties of the target image (Figure 6(a)), the S_2&L_2 reconstructed image (Figure 6(b)) and the *CCFs* reconstructed image (Figure 6(c)) were extracted by Eqs. (S4) and (S5). The extracted S_2 and L_2 values from Figs. 6(a, b) are compared and shown in Figure 6(d). Similarly, results for the extracted correlation function (S_2 and L_2) values from Figs. 6(a,b) are shown in Figure 6(e). Both in Figs. 6(d,e), it is clear that the S_2 of the reconstructed result matches the target data very well, indicating that their pore space distribution is very close. Similarly, the L_2 of the reconstructed result matches the target data very well, revealing that their pore size and connectivity state are very close.

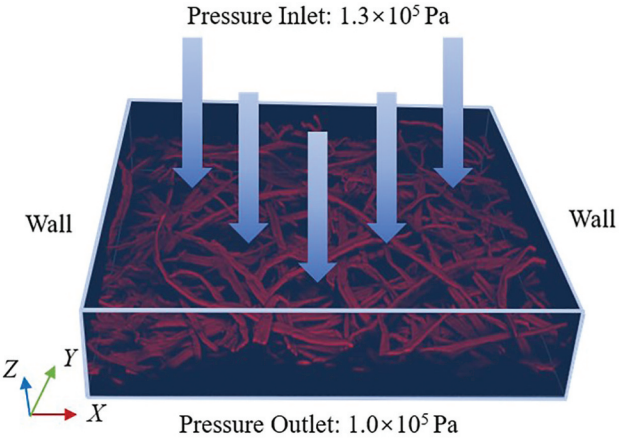

Figure 3. Boundary conditions of the simulation model for paper sheet.

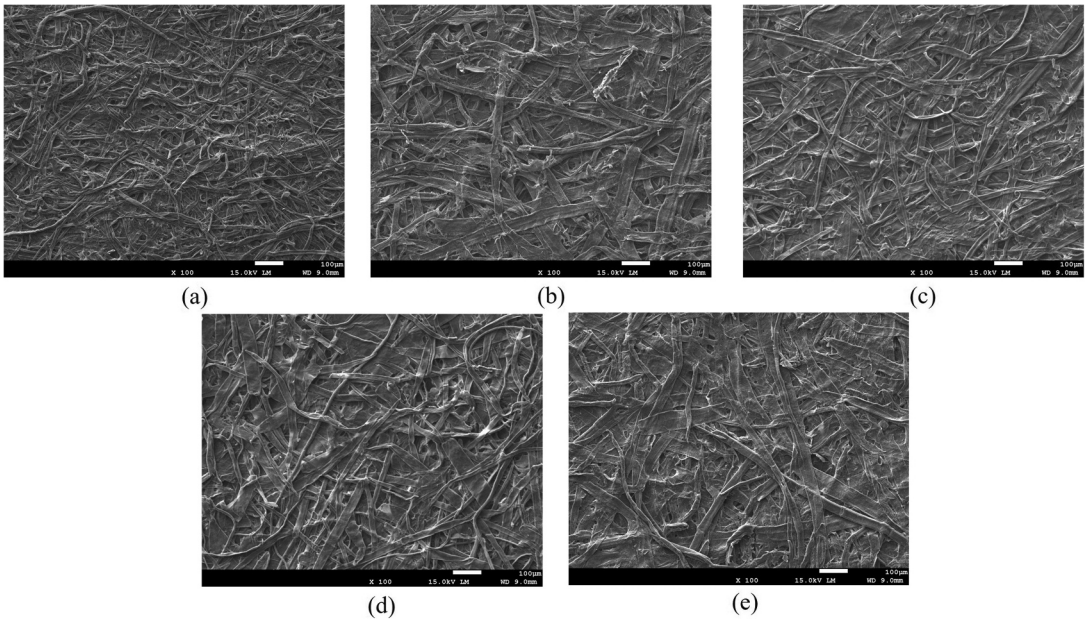

Figure 4. SEM images of the handsheets made by (a) eucalyptus, (b) masson pine, (c) bamboo, (d) bagasse, and (e) cotton.

The aforementioned study results demonstrate that, with the simulated annealing parameters in Table 1, the correlation functions S_2&L_2 and *CCFs* are effective and feasible in the 2D microstructure reconstruction for fiber and pore of paper sheet.

Comparison of 2D reconstruction with correlation functions S2&L2 and CCFs

To compare the reconstruction results with the correlation functions S_2&L_2 and *CCFs*, using the data from Figs. 6d,e, their reconstruction time and accuracy are listed in Table 2, in which the reconstruction accuracy was calculated by Eq. (S1) and expressed as an energy difference.

As presented in Figure 2, the SAR reconstruction time starts from the input of target image and terminates when the energy is less than the default minimum energy value $\Delta E_{\min} = 10^{-5}$. As listed in Table 2, based on the default minimum energy, the required reconstruction time for the methods of S_2

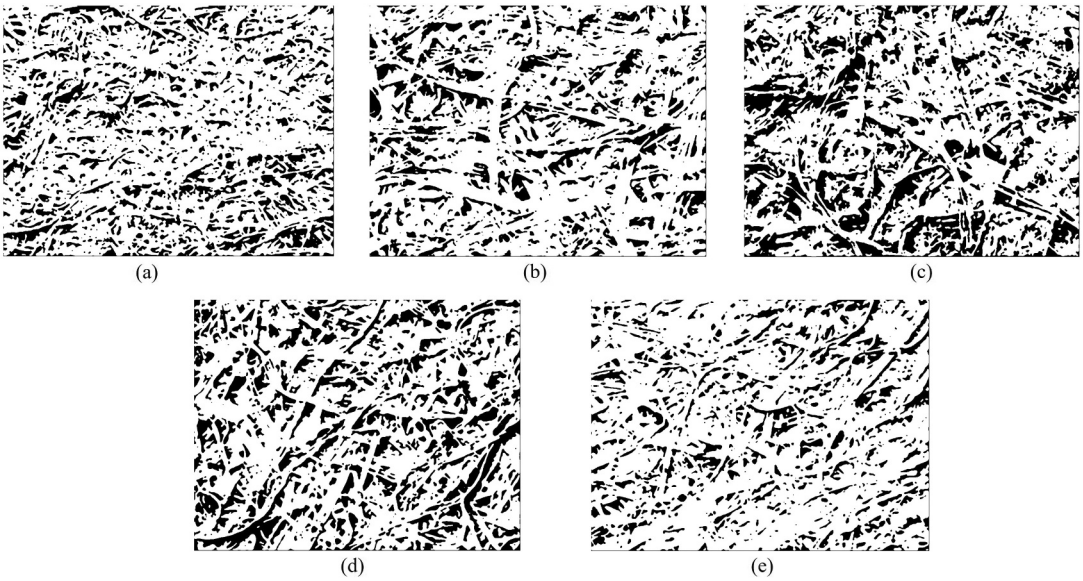

Figure 5. Binarized SEM images of the handsheets made by (a) eucalyptus. (b) masson pine. (c) bamboo. (d) bagasse. (e) cotton.

Table 1. Simulated annealing algorithm parameters.

Parameter	Symbols	Value
Distance of the S_2	r_d	20
Distance of the L_2	r_l	20
Distance of the *CCFs*	r_{ccf}	20
Monte Carlo (MC) step	k_{MC}	500
Temperature reduction factor	k	0.9
Maximum allowed failed iterations	k_{fail}	10^{-5}
Minimum energy	ΔE_{min}	10^{-5}
Minimum temperature	T_{min}	$10^{-30}\times T_{initial}$
Initial temperature of S_2&L_2 reconstruct	$T_{1,\ initial}$	10^{-5}
Initial temperature of *CCFs* reconstruct	$T_{2,\ initial}$	10^{-5}

&L_2 and *CCFs* are 3.67 and 2.07 min, respectively. The reconstruction time by the method *CCFs* is 43.37% lower than that by S_2&L_2. Besides, as for the reconstruction accuracy, both S_2 energy differences of S_2&L_2 and *CCFs* reconstruction results achieve 10^{-5} level, while their L_2 energy differences only reach 10^{-4} level, which is lower than the reconstruction accuracy with S_2. It means that the reconstruction accuracy for the distribution characteristics of pore (S_2) is higher than that for its connectivity (L_2).

Three-Dimensional reconstruction of paper sheets

Based on the 2D reconstruction results in Section 4.1, the two efficient reconstruction methods (S_2&L_2 and *CCFs*) were further employed to reconstruct the 3D microstructures of five types of handsheets and their reconstruction results were also compared.

3D reconstruction models with the correlation functions S2&L2 and CCFs

Due to the limitation of computing ability, the target size of the 3D reconstructed images by S_2&L_2 and *CCFs* was set as 100 × 100 × 100 voxels. Taking the paper sheet by bagasse pulp as an example, the 3D views of the reconstructed bagasse-sheet microstructures by S_2&L_2 and *CCFs* correlation functions are shown in Figure 7, respectively (details refer to S8.1 of SI). The 3D reconstructed views for the

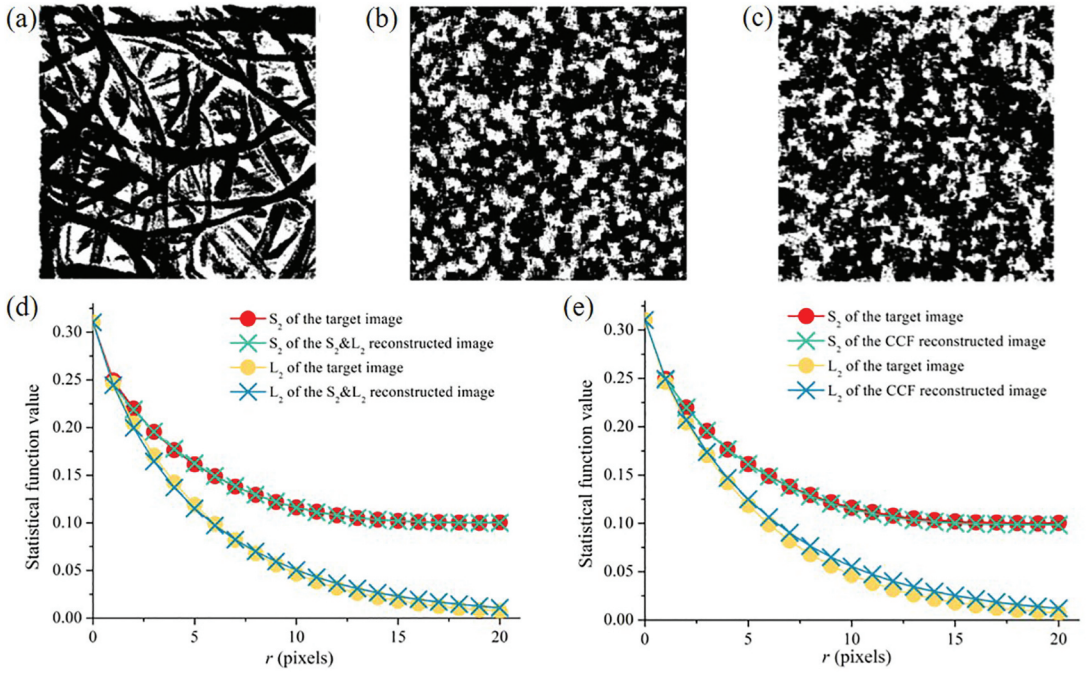

Figure 6. (A) SEM image of the bagasse handsheet (300*300 pixels), (b) 2D reconstruction image with the hybrid S_2&L_2 function, (c) 2D reconstruction image with *CCFs* function, (d) comparison of the correlation function values extracted from the images (a) and (b) by hybrid S_2&L_2 function, (e) comparison of the correlation function values extracted from the images (a) and (c) by *CCFs* function.

Table 2. Comparison of 2D reconstruction results with correlation functions S_2&L_2 and *CCFs* (for bagasse sheet).

Reconstruction methods	Reconstruction time (min)	S_2 energy difference	L_2 energy difference
S_2&L_2	3.67	2.98×10^{-5}	3.41×10^{-4}
CCFs	2.07	3.36×10^{-5}	9.17×10^{-4}

handsheets made of eucalyptus (Fig. S6), masson pine (Fig. S7), bamboo (Fig. S8), and cotton pulps (Fig. S9) are supplied in S8.2 of SI (Figure 8).

A comparison between the actual porosity and the computed one based on the 3D structure reconstruction is shown in Figure 9. It clearly demonstrates that, no matter what kinds of paper sheets are, their variation trends of the actual porosities and the computed ones based on the reconstructed structure are highly consistent. The porosity of the SEM image is one of the constraints in SAR, which makes the porosity of the 3D model from a large number of realizations (S_2&L_2 and *CCFs*) unchanged and the same as that of the SEM image (no error bars in Fig. 8.2). It is observed that the 3D reconstruction results of S_2&L_2 and *CCFs* are generally similar in macroscopic pore structure, but different with regard to the details from the views in Figure 7. To evaluate the reconstruction accuracy, using the SEM target images (Figure 5) and the generated 3D reconstruction models (S_2&L_2 and *CCFs*) as the inputs individually, their statistical geometric properties were extracted by Eqs (S4) and (S5). The extracted S_2 and L_2 values from the diverse inputs of the five types of samples are compared in Figure 8. Being similar to the 2D structure reconstruction, the reconstructed S_2 and L_2 values by these two kinds of reconstruction algorithms (S_2&L_2 and *CCFs*) are virtually indistinguishable from those of the targets. Thus, these comparison results indicate that the reconstructed 3D structure features reliably reproduce the 2D structure features of the handsheet, which were extracted from the analyzed SEM images.

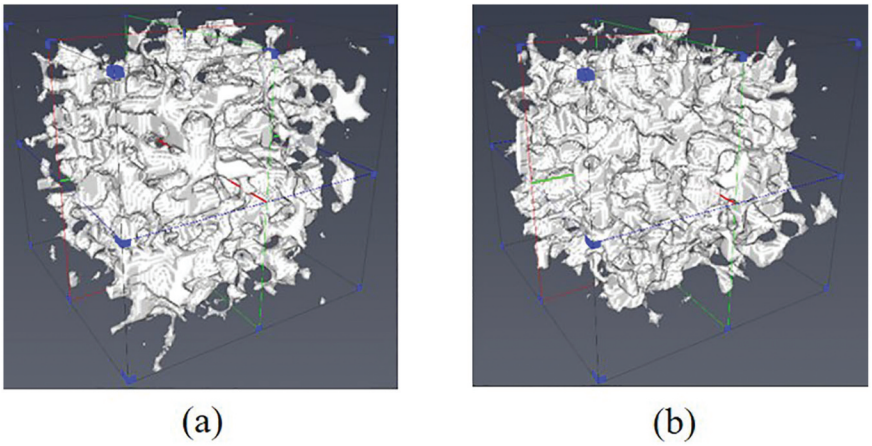

Figure 7. 3D views of reconstructed structures for bagasse handsheet by (a) hybrid S_2&L_2 function, (b) *CCFs* function.

Comparison of 3D reconstruction with correlation functions S2&L2 and CCFs

To compare the 3D reconstruction results with the correlation functions S_2&L_2 and *CCFs*, utilizing the data in Figure 8, their reconstruction times and accuracies based on the equative default minimum energy ($\Delta E_{\min} = 10^{-5}$) are listed in Table 3. The analyzed porosities of various handsheets were obtained from the binary image (Figure 5). Due to the complexity of 3D pore characteristics caused by piling up numerous 2D layers, much more reconstruction time is required for 3D reconstruction process than that required for 2D process. As displayed in Table 3, the consumed 3D reconstruction time ranges for S_2&L_2 and *CCFs* were [3.64–16.35 h] and [1.47–9.85 h], revealing that compared with the S_2&L_2 method, the reconstruction time by *CCFs* is shortened by 30–60%. It means that, while ensuring accuracy, the reconstruction efficiency is greatly improved and the running cost is saved by *CCFs* reconstruction method.

Besides, to investigate the relationship between paper porosity (analyzed from Figure 5), reconstruction time and accuracy clearly, the reconstruction results of different types of handsheet in Table 3 were further analyzed and plotted in Figure 10. As shown in Figure 10(a), by both methods of S_2&L_2 and *CCFs*, the reconstruction time basically increases with the increment of the paper sheet porosity, which is consistent with the technology analysis. In particular, when the porosity is greater than 26%, S_2&L_2 method takes more reconstruction time with the increment of porosity than that by *CCFs*. Therefore, *CCFs* are advantageous with respect to S_2&L_2 in reconstruction efficiency for microporous materials and more complex pore structures. As for the reconstruction accuracy analyzed in Figure 10(b), with the increase in porosity, the energy difference between the reconstructed images and target images with statistical features (S_2 and L_2) gradually widens. In particular, for the bagasse-sheet and cotton-sheet, possessing large porosities (31.38% and 32.94% in Table 3), their energy difference reaches 10^{-4} level (Table 3 and Figure 10(b)), which implies that the 3D reconstruction accuracy decreases with the increment of porosity.

Permeability simulation of 3D reconstruction

Concerning the transmission property of fibrous porous network, the most crucial criterion for characterizing the fluid behavior is the permeability which largely depends on its geometry. In the study, based on the reconstructed 3D pore structures with the correlation function *CCFs* for paper sheets in Table 3, an absolute permeability simulation was further conducted to investigate the fluid flowing behavior in the pores of the paper sheet.

Based on the simulation method in Section 3.2, using the water stream flowing through the five kinds of paper sheets in the thickness direction, under the boundary conditions defined in Figure 3, the

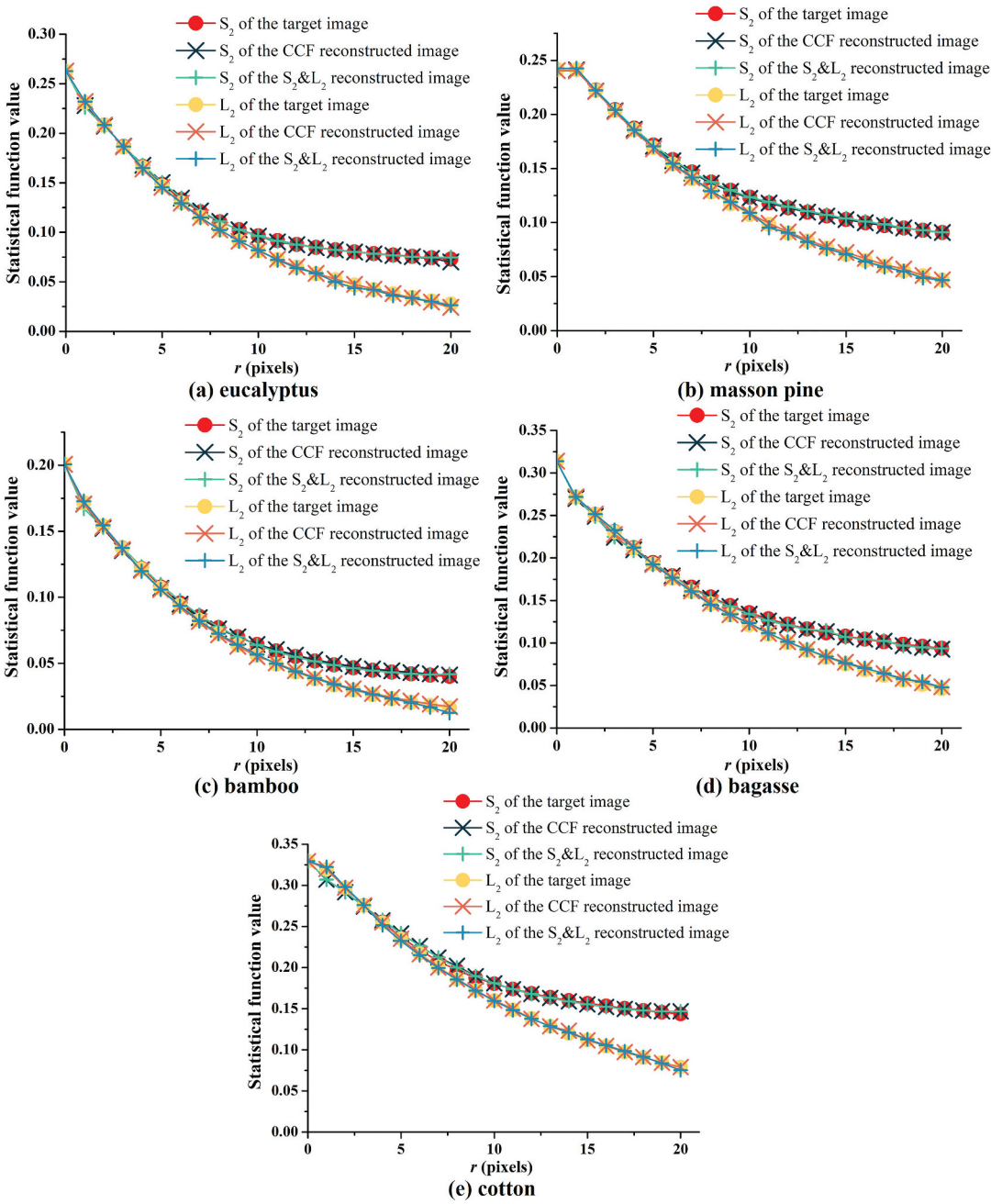

Figure 8. Comparison of S_2 and L_2 correlation functional values of the target images and the reconstructed microstructures for five types of handsheet.

permeability simulation results were obtained and presented in Figure 11. To quantify the simulated permeability of five kinds of paper sheets, calculating with Darcy's law given in Eq. (S10), the absolute permeability of different handsheets were obtained and shown in Figure 12.

In Figure 11, the black streamlines represent the route of water stream passing through paper sheets. It can be observed in Figure 11 that the fluid flows in the handsheets of eucalyptus (Figure 11(a)), bagasse (Figure 11(d)) and cotton (Figure 11(e)) are denser than those in masson pine (Figure 11(b))

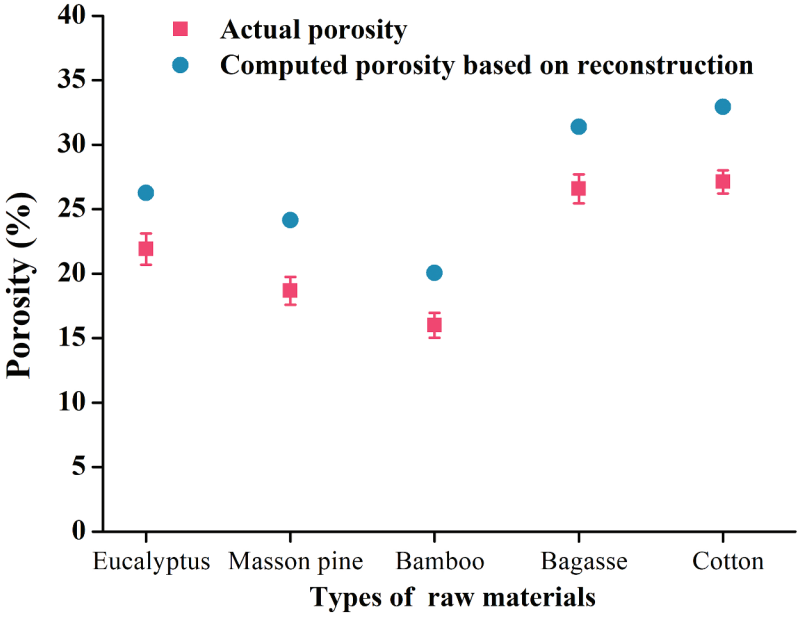

Figure 9. Comparison between the actual porosity and the computed porosity based on the 3D structure reconstruction.

Table 3. Comparison of 3D reconstruction results with correlation functions S_2&L_2 and *CCFs* (for five different paper sheets).

Types of Paper sheet	Analyzed Porosity (%)	Reconstruction Methods	Reconstruction Time (h)	Improvement of reconstruction efficiency (%)	Energy difference
Eucalyptus	26.27	S_2&L_2	8.63	30.82	5.92×10^{-5}
		CCFs	5.97		5.11×10^{-5}
Masson pine	24.15	S_2&L_2	5.08	43.11	6.34×10^{-5}
		CCFs	2.89		4.99×10^{-5}
Bamboo	20.07	S_2&L_2	3.64	59.62	5.58×10^{-5}
		CCFs	1.47		4.40×10^{-5}
Bagasse	31.38	S_2&L_2	14.97	37.07	1.18×10^{-4}
		-*CCFs*	9.42		1.25×10^{-4}
Cotton	32.94	S_2&L_2	16.35	39.76	3.33×10^{-4}
		CCFs	9.85		3.43×10^{-4}

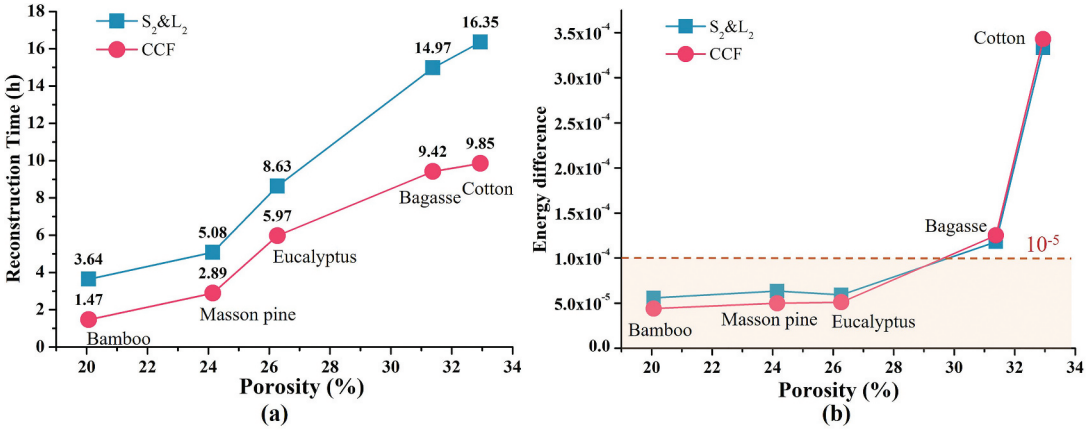

Figure 10. Comparison of 3D reconstructions of five kinds of handsheet. (a) reconstruction time, (b) reconstruction accuracy.

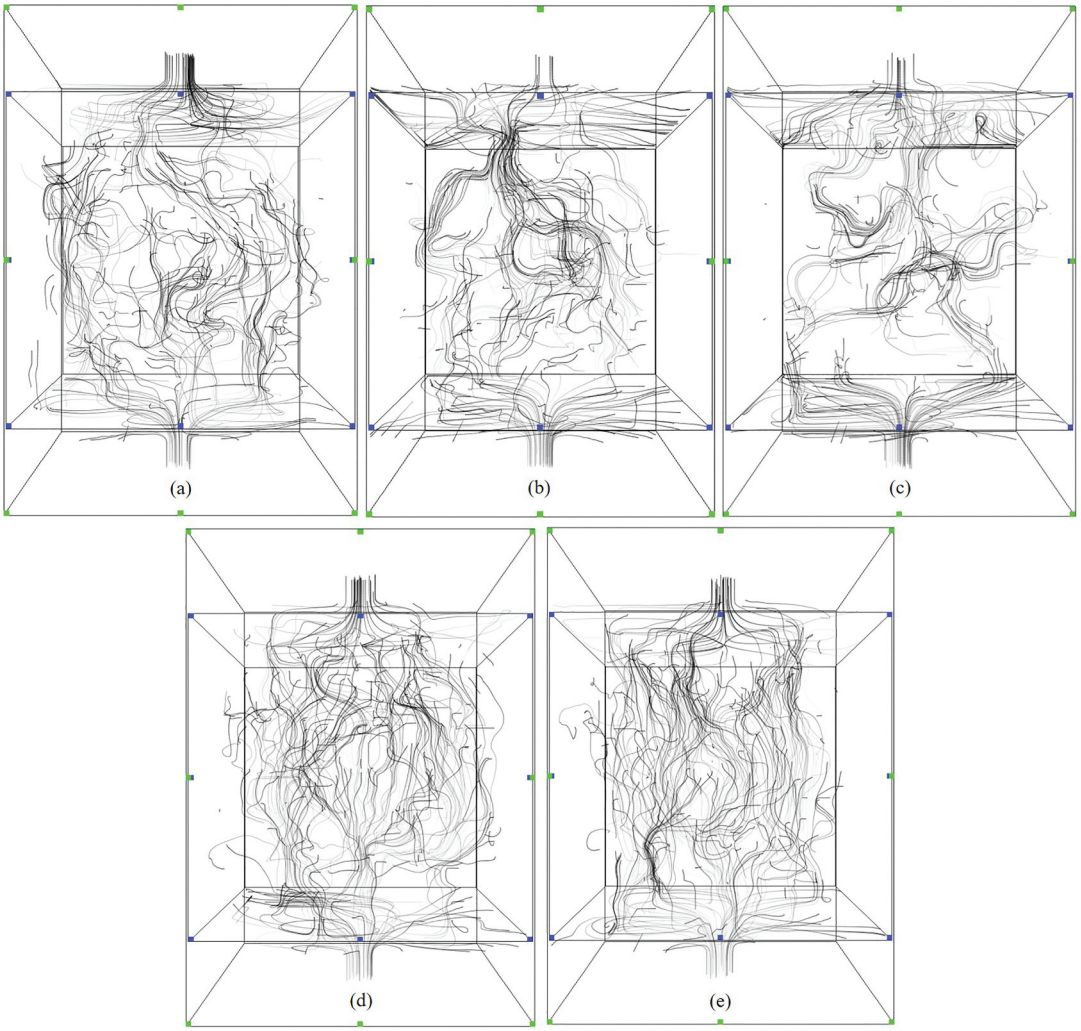

Figure 11. Permeability simulation results for five kinds of handsheets. (a) eucalyptus, (b) masson pine, (c) bamboo, (d) bagasse, and (e) cotton.

and bamboo (Figure 11(c)). Moreover, based on the simulation data in Figure 11, the calculated absolute permeability in Figure 12 reveals that the paper sheets made of eucalyptus, bagasse, and cotton have higher absolute permeability than those of masson pine and bamboo. It means that, if the porosity is large, the fluid paths are numerous and the streamlines are densely distributed, indicating a high absolute permeability. Besides, the experimental air permeability of paper sheets in Figure 12 displays the same results as those for calculated absolute permeability; in other words, the paper sheets made of eucalyptus, bagasse, and cotton have higher air permeability than those of masson pine and bamboo. The results of this study demonstrate that the permeability simulation of paper sheets can be verified with the experimental data, reflecting the difference between various raw materials.

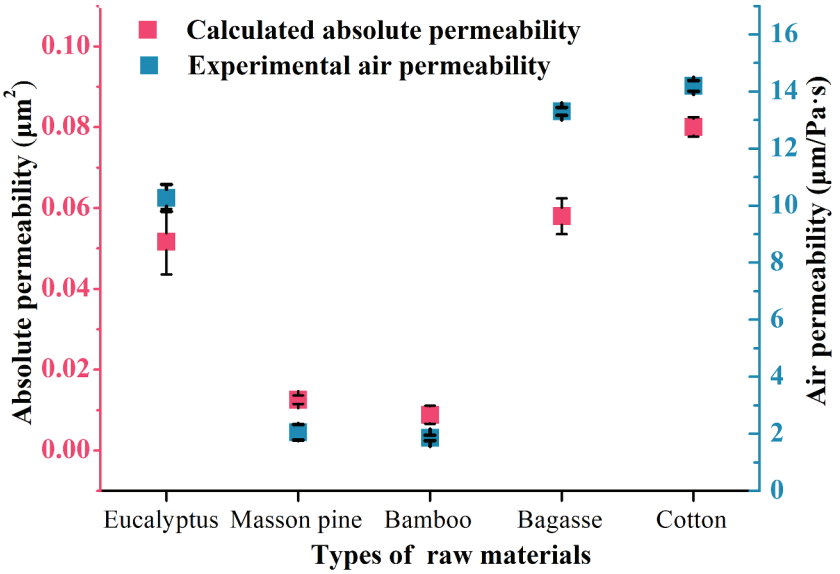

Figure 12. Calculated absolute permeability and the experimental air permeability of different paper sheets.

Conclusions and perspective

In this study, the simulated annealing reconstruction (SAR) method was employed to reconstruct the 3D fiber-pore structure of paper sheets. Five types of handsheets made of eucalyptus, masson pine, bamboo, bagasse, and cotton pulps were considered. Based on the binarized SEM images of five handsheets, the two-dimensional (2D) and three-dimensional (3D) reconstruction models were developed using the correlation functions S_2&L_2 and *CCFs*, respectively, and their reconstruction results were compared. Finally, penetration simulations and calculations of the absolute permeability of different handsheets were conducted. The following conclusions were obtained.

(1) Using the analyzed SEM images of handsheets as targets, with the S_2&L_2 and *CCFs* functions, the 2D reconstruction models of bagasse handsheet were developed in 3.67 min and 2.07 min with the correlation functions S_2&L_2 and *CCFs*, respectively, which shows that the efficiency of *CCFs* was 43.37% higher than that of S_2&L_2.
(2) The consumed 3D reconstruction time ranges for S_2&L_2 and *CCFs* were [3.64-16.35 h] and [1.47-9.85 h], showing that the reconstruction times by *CCFs* were shortened by 30–60% for 3D microstructure reconstruction. Besides, using both the correlation functions S_2&L_2 and *CCFs*, the extracted S_2 and L_2 values from the reconstructed 3D models were indistinguishable from those of the target SEM images, and the accuracy was basically at the level of 10^{-5}. These results demonstrated that, while ensuring accuracy, the reconstruction efficiency by *CCFs* method was higher.
(3) The visual permeability simulation results could reflect the structural difference of various handsheets with different pulps, and the trend of the calculated absolute permeability by Darcy's law were in agreement with that of the experimental air permeability, verifying the accuracy of permeability simulation.

The applicability and validity with SAR method to reconstruct the pore structure of paper sheet were revealed by the simulation results in the present study. Besides, it can be also used as a nondestructive characterization method for paper structure, playing an important role in its performance study. Furthermore, the present work can be strengthened by other efficient reconstruction methods in the future, such as the cross-correlation-based simulation method, which has been

considered as the most efficient method of multiple-point statistic reconstruction which can reconstruct nonstationary images.

Highlights

- Reconstruct virtual 3D microstructures of handsheets by analyzing 2D SEM images.
- Two-phase fiber-pore handsheets made of five different fibers are considered.
- Use two functions of S2&L2 and CCFs in a simulated annealing reconstruction method.
- Visual penetration simulations reflect structural differences of various handsheets.
- Calculated absolute permeability of handsheets agrees well with experimental values.

Acknowledgments

The authors appreciate the support provided by the Joint Research for International Cooperation on Scientific and Technological Innovation by MOST (2017YFE0184900) and the National Natural Science Foundation of Guangdong Province, China (2021A1515010327).

Disclosure statement

No potential conflict of interest was reported by the author(s).

Funding

This research was supported by the [Joint Research for International Cooperation on Scientific and Technological Innovation] under Grant [number 2017YFE0184900]; and [National Natural Science Foundation of Guangdong Province, China] under Grant [number 2021A1515010327].

Ethical approval

We confirm that all the research meets ethical guidelines and adheres to the legal requirements of the study country. The research does not involve any human or animal welfare-related issues.

References

Alexandersson, M., and M. Ristinmaa. 2021. Coupled heat, mass and momentum transport in swelling cellulose based materials with application to retorting of paperboard packages. *Applied Mathematical Modelling* 92:848–83. doi:10.1016/j.apm.2020.11.041.

Corson, P. B. 1974. Correlation functions for predicting properties of heterogeneous materials. II. Empirical construction of spatial correlation functions for two-phase solids. *Journal of Applied Physics* 45 (7):3165–70. doi:10.1063/1.1663742.

Costa, L. R., L. E. Silva, L. C. Matos, G. H. D. Tonoli, and P. R. G. Hein. 2021. Cellulose nanofibrils as reinforcement in the process manufacture of paper handsheets. *Journal of Natural Fibers*. Online publication: 1–16. doi:10.1080/15440478.2021.1958415.

Du, X. X., B. J. Xin, W. Chun, Y. Liu, F. L. Zhang, and J. H. Xu. 2021. Waterproof and moisture permeable nanofibrous membranes with multi-scale cross-linked structure. *Journal of Natural Fibers*. Online publication: 1–13. doi:10.1080/15440478.2021.1875355.

Esakkirajan, S., T. Veerakumar, A. N. Subramanyam, and C. H. PremChand. 2011. Removal of high density salt and pepper noise through modified decision based unsymmetric trimmed median filter. *IEEE Signal Processing Letters* 18 (5):287–90. doi:10.1109/lsp.2011.2122333.

Feng, J. X., Q. Z. Teng, X. H. He, L. B. Qing, and Y. Li. 2018. Reconstruction of three-dimensional heterogeneous media from a single two-dimensional section via co-occurrence correlation function. *Computational Materials Science* 144:181–92. doi:10.1016/j.commatsci.2017.11.030.

Gao, M. L., X. H. He, Q. Z. Teng, C. Zuo, and D. D. Chen. 2015. Reconstruction of three-dimensional porous media from a single two-dimensional image using three-step sampling. *Physical Review E* 91 (1). doi:10.1103/PhysRevE.91.013308.

Ghassemzadeh, J., M. Hashemi, L. Sartor, and M. Sahimi. 2001. Pore network simulation of imbibition into paper during coating: I. Model development. *AIChE Journal* 47 (3):519–35. doi:10.1002/aic.690470303.
Ghassemzadeh, J., and M. Sahimi. 2004a. Pore network simulation of fluid imbibition into paper during coating: II. Characterization of paper's morphology and computation of its effective permeability tensor. *Chemical Engineering Science* 59 (11):2265–80. doi:10.1016/j.ces.2004.01.057.
Ghassemzadeh, J., and M. Sahimi. 2004b. Pore network simulation of fluid imbibition into paper during coating - III: Modelling of the two-phase flow. *Chemical Engineering Science* 59 (11):2281–96. doi:10.1016/j.ces.2004.01.058.
Haralick, R. M., K. Shanmugam, and I. Dinstein. 1973. Textural features for image classification. *IEEE Transactions on Systems, Man, and Cybernetics* SMC-3 (6):610–21. doi:10.1109/TSMC.1973.4309314.
Jiao, Y., and N. Chawla. 2014. Modeling and characterizing anisotropic inclusion orientation in heterogeneous material via directional cluster functions and stochastic microstructure reconstruction. *Journal of Applied Physics* 115 (9):093511. doi:10.1063/1.4867611.
Jiao, Y., F. H. Stillinger, and S. Torquato. 2009. A superior descriptor of random textures and its predictive capacity. *Proceedings of the National Academy of Sciences of the United States of America* 106 (42):17634–39. doi:10.1073/pnas.0905919106.
Kim, S. Y., J. S. Kim, J. H. Lee, J. H. Kim, and T.-S. Han. 2021. Comparison of microstructure characterization methods by two-point correlation functions and reconstruction of 3D microstructures using 2D TEM images with high degree of phase clustering. *Materials Characterization* 172:110876. doi:10.1016/j.matchar.2021.110876.
Lin, B. B., Y. Bai, and B. X. Xu. 2021. Data-driven microstructure sensitivity study of fibrous paper materials. *Materials & Design* 197:109193. doi:10.1016/j.matdes.2020.109193.
Lu, B. L., and S. Torquato. 1992. Lineal-path function for random heterogeneous materials. II. Effect of polydispersivity. *Physical Review A, Atomic, Molecular, and Optical Physics* 45 (10):7292–301. doi:10.1103/physreva.45.7292.
Milanovic, J., T. Lazic, I. Zivkovic, M. Vuksanovic, M. Milosevic, and M. Kostic. 2020. The effect of nanofibrillated tempo-oxidized cotton linters on the strength and optical properties of paper. *Journal of Natural Fibers*. Online publication: 1–14. doi:10.1080/15440478.2020.1848742.
Moura, M. J., P. J. Ferreira, and M. M. Figueiredo. 2005. Mercury intrusion porosimetry in pulp and paper technology. *Powder Technology* 160 (2):61–66. doi:10.1016/j.powtec.2005.08.033.
Mukherjee, P. P., and C. Y. Wang. 2006. Stochastic microstructure reconstruction and direct numerical simulation of the PEFC catalyst layer. *Journal of the Electrochemical Society* 153 (5):A840–A849. doi:10.1149/1.2179303.
Pan, Z., X. Zhang, Z. Sun, F. Jiang, L. Lin, Y. Liang, M. Tang, and J. Wang. 2021. High fidelity simulation of ultrafine PM filtration by multiscale fibrous media characterized by a combination of X-ray CT and FIB-SEM. *Journal of Membrane Science* 620:118925. doi:10.1016/j.memsci.2020.118925.
Poletti, E., Z. Francesca, R. Alfredo, and G. Enrico. 2012. A review of thresholding strategies applied to human chromosome segmentation. *Computer Methods and Programs in Biomedicine* 108 (2):679–88. doi:10.1016/j.cmpb.2011.12.003.
Sahimi, M., and P. Tahmasebi. 2021. Reconstruction, optimization, and design of heterogeneous materials and media: Basic principles, computational algorithms, and applications. *Physics Reports-Review Section of Physics Letters* 939:1–82. doi:10.1016/j.physrep.2021.09.003.
Schiller, U. D., and F. Wang. 2018. Multiscale simulation of transport phenomena in porous media: From toy models to materials models. *MRS Communications* 8 (2):358–71. doi:10.1557/mrc.2018.29.
Strebelle, S. 2002. Conditional simulation of complex geological structures using multiple-point statistics. *Mathematical Geology* 34 (1):1–21. doi:10.1023/a:1014009426274.
Taghiyari, H. R., A. Kalantari, A. Kalantari, and S. Avramidis. 2019. Effect of wollastonite nanofibers and exposure to aspergillus niger fungus on air flow rate in paper. *Measurement* 136:307–13. doi:10.1016/j.measurement.2018.12.109.
Tahmasebi, P., and M. Sahimi. 2012. Reconstruction of three-dimensional porous media using a single thin section. *Physical Review E* 85 (6). doi:10.1103/PhysRevE.85.066709.
Tahmasebi, P., and M. Sahimi. 2013. Cross-correlation function for accurate reconstruction of heterogeneous media. *Physical Review Letters* 110 (7):078002. doi:10.1103/PhysRevLett.110.078002.
Tahmasebi, P., and M. Sahimi. 2016a. Enhancing multiple-point geostatistical modeling: 1. Graph theory and pattern adjustment. *Water Resources Research* 52 (3):2074–98. doi:10.1002/2015wr017806.
Tahmasebi, P., and M. Sahimi. 2016b. Enhancing multiple-point geostatistical modeling: 2. Iterative simulation and multiple distance function. *Water Resources Research* 52 (3):2099–122. doi:10.1002/2015wr017807.
Torquato, S., J. D. Beasley, and Y. C. Chiew. 1988. Two-point cluster function for continuum percolation. *The Journal of Chemical Physics* 88 (10):6540–47. doi:10.1063/1.454440.
Wang, S. H., and Y. D. Gao. 2021. Preparation of cotton fiber-derived porous-carbon materials and their application as high-performance supercapacitors. *Journal of Natural Fibers*. Online publication. doi:10.1080/15440478.2021.1944436.
Whitaker, S. 1986. Flow in porous media I: A theoretical derivation of Darcy's law. *Transport in Porous Media* 1 (1):3–25. doi:10.1007/BF01036523.
Wu, W., and F. M. Jiang. 2013. Simulated annealing reconstruction and characterization of a $LiCoO_2$ Lithium-ion battery cathode. *Chinese Science Bulletin* 58 (36):4692–95. doi:10.1007/s11434-013-6095-5.

Yeong, C. L. Y., and S. Torquato. 1998a. Reconstructing random media. *Physical Review E* 57 (1):495–506. doi:10.1103/PhysRevE.57.495.

Yeong, C. L. Y., and S. Torquato. 1998b. Reconstructing random media. II. Three-dimensional media from two-dimensional cuts. *Physical Review E* 58 (1):224–33. doi:10.1103/PhysRevE.58.224.

Zachary, C. E., and S. Torquato. 2011. Improved reconstructions of random media using dilation and erosion processes. *Physical Review E* 84 (5):056102. doi:10.1103/PhysRevE.84.056102.

Zhang, Y. X., F. Y. Yan, M. F. Yan, Y. H. Wan, Z. J. Jiao, C. R. Xia, F. L. Chen, and M. Ni. 2019. High-throughput, super-resolution 3D reconstruction of nano-structured solid oxide fuel cell electrodes and quantification of microstructure-property relationships. *Journal of Power Sources* 427:112–19. doi:10.1016/j.jpowsour.2019.04.065.

Zhou, M. J., M. Z. Fang, Z. Z. Quan, H. N. Zhang, X. H. Qin, R. W. Wang, and J. Y. Yu. 2019. Large-scale preparation of micro-gradient structured sub-micro fibrous membranes with narrow diameter distributions for high-efficiency air purification. *Environmental Science-Nano* 6 (12):3560–78. doi:10.1039/c9en00816k.

Zhou, X. P., and N. Xiao. 2018. 3D numerical reconstruction of porous sandstone using improved simulated annealing algorithms. *Rock Mechanics and Rock Engineering* 51 (7):2135–51. doi:10.1007/s00603-018-1451-z.